Alkali subhalides: high-pressure stability and interplay between metallic and ionic bonds†

G. Saleh*[a] and A. R. Oganov[abcd]

The application of high pressure (hundreds of gigapascals) to materials, besides modifying their properties, changes dramatically their reactivity. Consequently, new compounds are formed, which violate the chemical paradigms known to date. In fact, it was recently discovered (Zhang *et al.*, *Science*, 2013) that sodium subchlorides (Na_xCl, $x > 1$) become stable at high pressure. In this work, we carry out a thorough study of these compounds as well as of other alkali subhalides by means of evolutionary crystal structure prediction calculations combined with an in-depth analysis of their crystal and electronic structures. The results of our investigation are threefold. We present an updated phase diagram of Na_xCl, including one new compound (Na_4Cl_3) and two previously undiscovered phases of Na_3Cl. We demonstrate the appearance of remarkable features in the electronic structure of sodium subchlorides, such as chlorine atoms acquiring a -2 oxidation state. Most importantly, we derive a model which enables one to rationalize the stability of alkali subhalides at high pressure. The predictive ability of our model was validated by the results of crystal structure prediction calculations we carried out on alkali subhalides A_3Y (A = Li, Na, K; Y = F, Cl, Br). Moreover, we show how the stability of recently reported high-pressure compounds can be rationalized on the basis of the insights gained in the present study.

1. Introduction

When materials are subjected to pressures of tens or hundreds of gigapascals (GPa), their physicochemical properties undergo dramatic changes.[1] Concomitantly, new chemical compounds are formed because of the increased reactivity of certain elements and compounds.[2] The interest towards high-pressure phenomena has strongly risen in the last decades thanks to the development of experimental apparatuses capable of reaching very high pressures and, contemporaneously, to the advent of reliable computational approaches for crystal structure prediction. This parallel evolution of theoretical and experimental techniques for high-pressure materials science has revealed a completely novel realm

of chemistry. Indeed, new phenomena, unexpected on the basis of ambient-pressure chemistry, were brought to light. Reactivity of noble gases,[3] metal-to-insulator transition[4] and participation of inner electronic shells in chemical bonding[5] are but a few examples of how the paradigms of chemistry established in the last century need to be modified when pressure comes into play. Detailed descriptions of the high-pressure behavior of materials are nowadays available (see, for example, ref. 1, 6 and references therein). On the other hand, the field of high-pressure chemistry is still in its infancy, as predicting the abovementioned phenomena, even at a qualitative level, is not yet possible.

An interesting discovery regarding the high-pressure behavior of rocksalt recently appeared in literature.[2] It was observed that when an external pressure greater than 20 GPa is applied, NaCl becomes reactive towards its own components and forms thermodynamically stable compounds of general formulae Na_xCl (x = 1.5, 2, 3) and $NaCl_y$ (y = 3, 7). These compounds were discovered by *ab initio* crystal structure prediction calculation using the USPEX code,[7] and their formation was subsequently verified experimentally. Clearly, the stability of such compounds clashes against the basic rules of chemistry. The Na-rich side of the Na_xCl_y phase diagram, corresponding to sodium subchlorides, is particularly intriguing for it includes four compositions (Na_4Cl_3 is presented here for the first time) and a wealth of different crystal structures. A physically rooted explanation about how pressure acts in stabilizing these odd compounds is still lacking.

[a] *Moscow Institute of Physics and Technology, 9 Institutskiy Lane, Dolgoprudny city, Moscow Region, 141700, Russia. E-mail: gabrielesaleh@outlook.com*

[b] *Skolkovo Institute of Science and Technology, Skolkovo Innovation Center, 3 Nobel St., Moscow 143026, Russia*

[c] *Department of Geosciences and Department of Physics and Astronomy, Stony Brook University, Stony Brook, New York 11794-2100, USA*

[d] *School of Materials Science, Northwestern Polytechnical University, Xi'an, 710072, China*

In this work, we present a thorough study of the crystal and electronic structures of alkali subhalides. We investigate the chemical bonding pattern of sodium subchlorides by analyzing their geometry, density of states (DOS), total charge density (in the framework of the Quantum Theory of Atoms In Molecules, QTAIM[8]), deformation density and electron localization function (ELF[9]) distributions. These approaches are briefly reviewed in Section 2.1. The results obtained allowed us to single out those structural and electronic factors responsible for the stability of the various high-pressure phases of Na_xCl. In order to test the predictive ability of the model we put forward, we carried out crystal structure prediction calculations on 9 alkali subhalides A_3Y (A = Li, Na, K; Y = F, Cl, Br) in the pressure range 0–350 GPa. These calculations were afforded through the use of the powerful evolutionary method implemented in the USPEX code.[7] We analyzed chemical bonding in the resulting structures by employing the same approaches adopted for sodium subchlorides. Moreover, we show how the proposed model can be extended beyond alkali subhalides by discussing its application to recent results on the Mg–O, Na–Bi, and Li–B systems at high pressure. Last but not least, we present an updated version of the Na_xCl phase diagram, which includes three novel phases and one new compound, Na_4Cl_3.

2. Theoretical background and computational methods

2.1. Theoretical background

QTAIM establishes a quantum-mechanically rooted link between topological features of the electron density distribution and fundamental chemical concepts such as atoms and bonds.[8] The latter are associated to the appearance of the so-called 'bond critical points' (bcp's). Values of certain scalar fields, such as the electron density and energy density at the bcp provide precious information about the type of interaction (ref. 10). We adopted the existence of a bcp as unbiased criterion to determine the coordination sphere of a given atom. Regarding atoms, QTAIM introduces an exhaustive and quantum-mechanically rooted partitioning of space into atomic basins, the latter being separated by the so-called 'zero-flux surfaces'. All the properties of a system can then be decomposed into atomic contributions. By their mathematical definition, zero-flux surfaces must contain one and only one electron density maximum, which is usually found on nuclei. However, in some cases, non-nuclear maxima of charge density are known.

ELF is considered as "a simple measure of electron localization"[9] and is defined in terms of a Taylor expansion of the spherically-averaged same-spin pair probability density through the following formula:

$$\eta(\mathbf{r}) = \left\{ 1 + \left[\left(\sum_i^{N_{orb}} |\nabla \varphi_i(\mathbf{r})|^2 - \frac{|\nabla \rho(\mathbf{r})|^2}{8\rho(\mathbf{r})} \right) \middle/ \left(\frac{3}{10}(3\pi^2)^{\frac{2}{3}} \rho(\mathbf{r})^{\frac{5}{3}} \right) \right]^2 \right\}^{-1} \quad (1)$$

where $\rho(\mathbf{r})$ is the electron density at $\mathbf{r}$, φ_i is the i-th canonical orbital and the summation runs over all the (doubly) occupied orbitals. The Lorentzian form of the ELF expression guarantees that ELF values are bounded between 1 and 0, corresponding respectively to maximal and minimal localization with respect to a uniform electron gas having the same electron density. From a chemical perspective, ELF maxima, and the associated basins (defined through zero-flux surfaces, similarly to QTAIM), correspond to either core or valence electrons. The latter types of basins are particularly informative, as they convey important information about lone pairs, unpaired electrons (for magnetic systems), and chemical bonds.[11] In this work, we characterize valence ELF basins by considering three features: ELF values within the basin (average and maximum), the number of electrons contained in the basin (and the related average charge density), and its synaptic order δ. The latter, which is defined as the number of core basins a given valence basin shares a surface with, allows one to discern among lone pairs ($\delta = 1$), 2-center bonds ($\delta = 2$), and multicenter bonds ($\delta > 2$).

The deformation density is the difference between the charge density of a given structure and the corresponding procrystal density. The latter is obtained as the superposition of spherical, neutral, atomic densities centered at the equilibrium positions of the atoms. Deformation density enables one to study the rearrangement of charge density due to the formation of chemical bonds and/or to the response of the system to the applied pressure.

2.2. Computational methods

All the calculations mentioned in this work were carried out within density functional theory. The exchange–correlation functional of Perdew–Burke–Ernzerhof[12] was adopted throughout. We performed two types of periodic calculations, which differ in the way in which the Bloch functions are expanded: projector augmented plane waves[13] and (all-electron) atom-centered Gaussian functions, as implemented in the codes VASP[14] and CRYSTAL14,[15] respectively. Plane-wave calculations were adopted for crystal structure predictions and for geometry optimizations. Single point calculations were then performed with CRYSTAL14 and the resulting wavefunctions were exploited for chemical bonding analysis. For plane-wave calculations, small-core PAW potentials, high plane-wave kinetic energy cutoffs and dense sampling of the reciprocal space were adopted in order to obtain accurate results. The basis set for CRYSTAL14 calculations was taken from ref. 16 ('triple-zeta plus polarization' quality, optimized for solid-state calculations) and slightly modified for applications to high pressure. Since for some systems non-nuclear charge density maxima were found, when not otherwise specified, additional basis functions centered on those maxima were added. A very dense sampling of the reciprocal space, as well an extremely fine (unpruned) grid for DFT calculations were used. Particular care was taken in tuning the contraction of the basis functions so as to obtain physically meaningful orbital projections in p-DOS plots (see ESI 1.2†). In general, we found a very good agreement between DOS evaluated with CRYSTAL14 and with VASP

This journal is © the Owner Societies 2016

Phys. Chem. Chem. Phys., 2016, **18**, 2840–2849 | **2841**

(some examples are reported in Fig. S1, ESI†). The integration of quantities within zero-flux ELF surfaces, not implemented in CRYSTAL14, was performed by means of the code critic2[17] exploiting the grid-based Yu–Trinkle algorithm.[18] For more details on computational parameters, see Section ESI 1.†

Crystal structure predictions were done with the USPEX code.[19,20] For all A_3Y (A = Li, Na, K; Y = F, Cl, Br) compounds, USPEX calculations at 100, 200 and 350 GPa were carried out. Additional crystal structure predictions at other pressures were performed on some compounds depending on the results of the aforementioned calculations (see Section ESI 1.4†). On top of that, we exploited the USPEX code to explore the Na_xCl phase diagram at various pressures. Geometry optimizations on the resulting most stable structures were then performed in the pressure range 0–350 GPa. Crystal structures of high-pressure phases of Li, Na, and K were taken from ref. 21, 22 and 23 respectively. For alkali halides AY, we considered, besides B1 and B2 phases, the structures reported in ref. 24–26. Since KF, KBr and NaBr undergo B1–B2 transition at low pressure, we ran USPEX calculations on these compounds in order to explore the possibility of the formation of other structures at higher pressures (KCl was already explored in ref. 24 and 26). However, the resulting structures belonged to already reported structure types.

Phonon dispersion curves were computed with the PHONOPY code.[27] Visualizations were performed with the codes Diamond[28] and VESTA.[29]

3. Results and discussion

3.1. Sodium subchlorides: structure and bonding

In this section we discuss chemical bonding in the thermodynamically stable sodium subchlorides Na_xCl (x = 1.33, 1.5, 2, 3). For a given pressure, we deem a phase 'thermodynamically stable' when its enthalpy of formation from elements or any other possible compound is negative. Crystal structures are depicted in Fig. 1 and 6c ($Cmmm$-Na_2Cl), whereas more detailed pictures, including the positions of Na–Cl bcp's, are reported in ESI† (Fig. S5 and S14). In Fig. 2 we show the updated phase diagram of Na_xCl, which includes three new structures: $P2_1/c$-Na_3Cl, $R\bar{3}m$-Na_3Cl and $R\bar{3}$-Na_4Cl_3.‡ All of them are dynamically stable, as indicated by the absence of imaginary frequencies in all the phonon dispersion curves (Fig. S2–S4 of ESI†).

The two lowest-pressure structures of Na_3Cl can be viewed as formed by alternating layers of NaCl and of pure Na (Fig. 1a and b). These Na layers will be referred to as '2D-Na sublattice' in the rest of the paper. Similarly, one-dimensional sublattices of sodium, hereinafter named 1D-Na, can be identified in $P4/m$-Na_3Cl_2, $Cmmm$-Na_2Cl and $R\bar{3}m$-Na_3Cl. In the very high-pressure

‡ Note that, differently to what reported in ref. 2, our calculations indicate that $P4/mmm$-Na_2Cl and $Imma$-Na_3Cl_2 are not stable. $P4/mmm$-Na_2Cl is less stable with respect either to other Na_2Cl phases (p > 128 GPa) or to the Na_3Cl + NaCl mixture (p < 128 GPa). The same holds true for $Imma$-Na_3Cl_2 when compared to other Na_3Cl_2 phases (p < 170 GPa) or to the Na_4Cl_3 + Na_2Cl mixture (p > 170 GPa), vide infra. Several computational settings were tested (e.g. different pseudopotentials and plane wave energy cutoffs): with none of them were $P4/mmm$-Na_2Cl and $Imma$-Na_3Cl_2 stable.
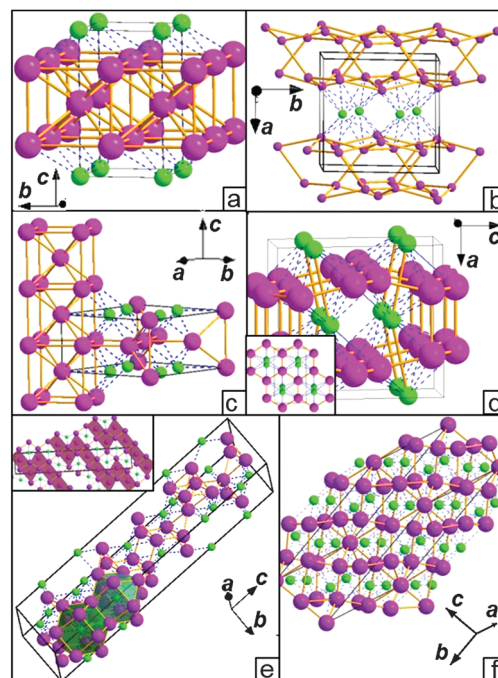

Fig. 1 Crystal structures of sodium subchlorides. (a) $P4/mmm$-Na_3Cl (b) $P2_1/c$-Na_3Cl (Na atoms are drawn smaller for clarity) (c) $P4/m$-Na_3Cl_2 (d) $Imma$-Na_2Cl (inset: projection along the a axis) (e) $R\bar{3}m$-Na_3Cl (f) $R\bar{3}$-Na_4Cl_3. Unit cells shown as black solid lines. In (e) we explicitly show the two symmetry-independent Cl–Na polyhedra. Moreover, in the inset the (distorted) Na-bcc blocks are highlighted (projection along b axis). In this and all the other pictures, Na and Cl atoms are colored in violet and green, respectively.
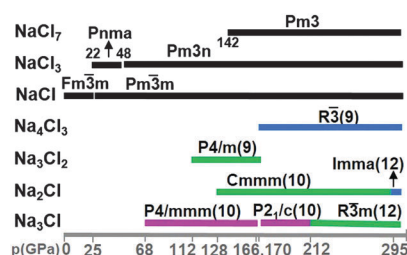

Fig. 2 Updated composition-pressure phase diagram of the Na–Cl system. For $NaCl_y$ (y > 1) compounds, the data were taken from ref. 2. The transition/formation pressures are indicated near each bar. For Na_xCl (x ≥ 1) compounds, instead, the pressure bar reported at the bottom contains the values at which new phases become stable. 166 and 170 GPa refer respectively to $P2_1/c$-Na_3Cl and $R\bar{3}m$-Na_4Cl_3. The number in brackets indicates the anion–cation coordination (see main text). For alkali subhalides, the color of the bars represents the type of sodium sublattice: 2D (violet), 1D (green), no Na–Na bonds (blue).

polymorphs of Na_2Cl and Na_4Cl_3, sodium atoms are arranged in flat layers, and such sublattices cannot be identified. In the following, we will show how the presence/absence and the type (1D-Na vs. 2D-Na) of the aforementioned sodium sublattices univocally correspond to a given chemical bonding pattern. In the next section, we will analyze the relationship among the external pressure, the formation (and disruption) of sodium sublattices and the stability of sodium subchlorides.

2D-Na sublattices are present in the $P4/mmm$ and $P2_1/c$ forms of Na$_3$Cl. Both are metallic, as can be inferred from their DOS plots (Fig. S6 and S7, ESI†). The Fermi level, however, falls within a pseudogap. In order to rationalize the stability of these and the other compounds (see *infra*), we interrogate ourselves as to the chemical origin of their valence states. The answer to this question comes from the analysis of p-DOS and of the spatial distribution of the charge density associated to the valence states (hereinafter 'valence density'). The valence band is mostly formed by sodium orbitals and the corresponding density is located inside the 2D-Na layers (Fig. S6 and S7, ESI†). Hence, sodium atoms form metallic bonds in 2 dimensions. Next we analyse the valence ELF distribution. The latter is arranged, within Na layers, in polysynaptic basins ($\delta = 4$ for $P4/mmm$-Na$_3$Cl and $\delta = 10$ $P2_1/c$-Na$_3$Cl) whose maxima are located in the interstices between atoms (Fig. 3b). This is a typical signature of metallic bonds.[30] The relatively simple structure of $P4/mmm$-Na$_3$Cl, whose 2D-Na layers are composed of (distorted) Na-bcc units, allows a direct comparison with the pure metal (Fig. 3a and b). Compared to pure Na-bcc, 2D-Na layers display a smaller number of basins, which are characterized by a higher total electron population and higher values of ELF and charge density. These results indicate a stronger localization of valence electrons in 2D-Na sublattices compared to pure bcc-Na. We also see that mobile electrons belong to the inner part of the Na layers. Regarding chlorine, its valence ELF is arranged in monosynaptic basins whose population sums up to 8 electrons, a feature characteristic of plain Cl$^-$ anions (*e.g.* in NaCl). The electron count of ELF basins shows, as expected, that the 2D-Na layers are positively charged, as one in every three electrons is transferred to Cl atoms. The ELF distribution in $P2_1/c$ is quite similar to the one in $P4/mmm$-Na$_3$Cl, the main difference being that in the former the poly-synaptic basins within the 2D-Na layers have higher synaptic order, higher electron population and higher ELF value (Fig. S7, ESI†). This is because upon the $P4/mmm \rightarrow P2_1/c$ transition, the 2D-Na sublattice rearranges and form more closely packed layers, as discussed in the next section. The analysis of deformation density distribution (Fig. S6 and S7, ESI†) reveals qualitatively the same information obtained from ELF, thereby further supporting the chemical bonding description given

above. Overall, the picture that emerges from ELF and DOS analyses is that in Na$_x$Cl compounds containing 2D-Na sub-lattices, these can be described as positively charged metallic layers interacting electrostatically with Cl$^-$ anions.

This description is corroborated by QTAIM atomic properties (Table 1). In fact, Cl atoms display a volume and charge slightly greater than in NaCl. However, this is due to the increased number of electropositive sodium atoms in the coordination sphere of chlorine, and the atomic properties of chlorine are to a great extent similar to the ones observed in NaCl. Na atoms, on the other hand, bear a smaller positive charge than in NaCl, because these atoms in Na$_3$Cl are involved at the same time in electrostatic and metallic interactions. This hypothesis is confirmed by the analysis of scalar properties evaluated at bcp's of both $P4/mmm$ and $P2_1/c$ structures of Na$_3$Cl: Na–Na bcp's within the 2D-Na layers bear all the typical features of covalent (metallic, in this case) bonds, while Na–Cl bcp's properties are typical of closed-shell interactions (Fig. S5 and S14, ESI†).

1D-Na sublattices are composed of distorted Na-bcc units in all three compounds where they are present. In $Cmmm$-Na$_2$Cl and $R\bar{3}m$-Na$_3$Cl, such sublattices cross each other, giving rise to 2- and 3-dimensional nets of 1D-Na strands, respectively (Fig. S15, ESI†). The transition from 2D-Na layers to 1D-Na strands leads to the formation of additional Na/NaCl inter-faces. The latter, in turn, further enhances the localization of electrons inside the 1D-Na sublattice. Indeed, the merging of ELF basins and the corresponding increased electron localiza-tion (as measured by ELF and charge density values within valence basins) observed in passing from Na-bcc to 2D-Na layers of $P4/mmm$-Na$_3$Cl, takes place also in passing from the latter to 1D-Na motifs (Fig. 3c). In particular, the 4 ELF basins detected within the bcc units of 2D-Na layers merge into one unique basin.§

The localization of electrons is also reflected in the topology of charge density, as (non-nuclear) maxima appear in the same interstitial positions as the ELF maxima shown in Fig. 3c. This interstitial electron localization leads to a dampening of the metallic character. Indeed, the Na$_x$Cl phases formed by 1D-Na sublattices are either poorly conducting or zero-gap semi-conductors, as inferred from their DOS plots (an example is reported in Fig. 4). Analysis of p-DOS and valence density distribution (Fig. 4) shows how the interstitial electrons within the 1D-Na strands give rise to a sharp peak in the valence region of the DOS. The conduction band, instead, is mainly formed by Cl orbitals. A significant contribution from Cl atoms to the valence band is also present and is due to partially occupied d-orbitals. The extra charge acquired by Cl atoms is mirrored in a
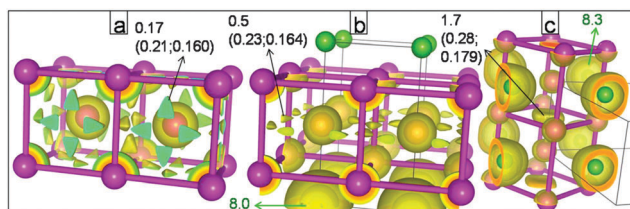

Fig. 3 ELF isosurfaces of selected compounds at 125 GPa. (a) Na-bcc, (b) $P4/mmm$-Na$_3$Cl, (c) $P4/m$-Na$_3$Cl$_2$. We adopted isovalues (0.38, 0.63 and 0.84 for a, b and c respectively) close to the value of ELF maxima in polysynaptic basins. For the latter, we report their electron population and, in brackets, average ELF and average electron density (a.u.), in this order. Green numbers indicate the valence population of Cl atoms (*i.e.* the sum of their monosynaptic basins).

§ Actually, at moderate pressures, 4 ELF maxima in the shape of a square can be distinguished. However, the latter are very close to each other and the difference in the ELF value between the maximum and the saddle points is very small. For example, for Na$_3$Cl$_2$ at 200 GPa, the distance between maxima is lower than 0.5 Å, while the ELF values are 0.944 0.942 0.932 respectively for the maxima, the first-order saddle points joining them and the second order saddle point at the center of the square. From a chemical bonding point of view, such an ELF distribution should be considered as a unique basin, as discussed, for example, in: A. Savin, *Journal of Molecular Structure*, 2005, **727**, 127–131.

This journal is © the Owner Societies 2016

Phys. Chem. Chem. Phys., 2016, **18**, 2840–2849 | **2843**

Table 1 QTAIM atomic properties for selected compounds (full list in Table S2, ESI)

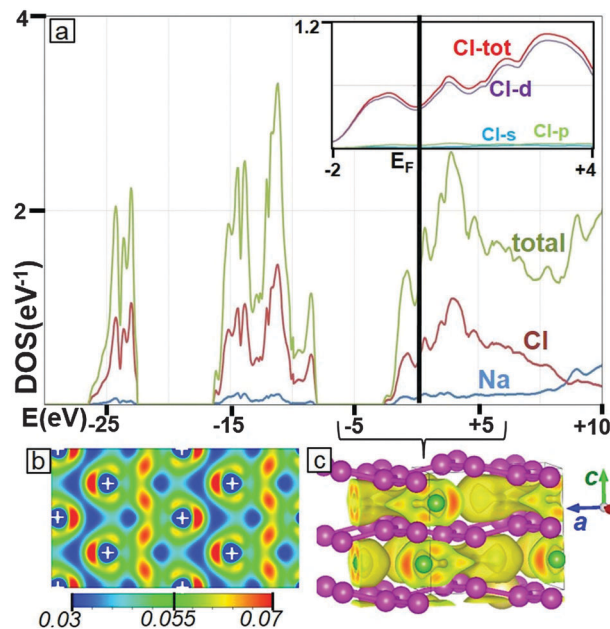| Compound (pressure)	Atom	Charge	Volume [a.u.]
Na_3Cl-$P4/mmm$ (125 GPa)	Na1	0.19	58.3
	Na2	0.36	51.1
	Cl	−0.91	101.8
Na_2Cl-$Imma$ (300 GPa)	Na	0.66	29.2
	Cl	−1.32	81.6
NaCl-$Pm3m$ (125 GPa)	Na	0.77	36.5
	Cl	−0.77	96.5
NaCl-$Pm3m$ (300 GPa)	Na	0.75	29.0
	Cl	−0.75	73.2
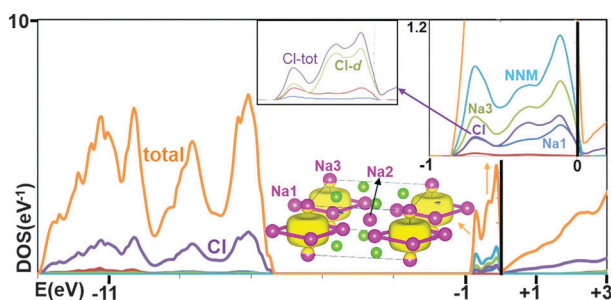
Fig. 4 p-DOS plot for $P4/m$-Na_3Cl_2 at 125 GPa. Fermi level is indicated as vertical black line. NNM represents the contribution from the basis functions centered on non-nuclear maxima. Valence charge density isosurfaces (0.01 a.u.) are shown at the center. Insets: Atomic contributions to valence band (top right, the contribution of Na2 is lower than 0.05 eV^{-1}, hence it is not labelled) and orbital partitioning of chlorine contribution (top, center).

Fig. 5 p-DOS (a) and partial density plots (b and c) for $Imma$-Na_2Cl at 300 GPa. In (a), the inset shows the projection onto Cl atomic orbitals. The charge density corresponding to the energy interval −5 eV, +5 eV (with respect to the Fermi level E_F) is plotted in the (001) plane (2×2 supercell) (b) and as 0.05 a.u. isosurface (c). Note that the (001) plane passes through the Cl atoms, which are shown in b as white crosses.

valence ELF population greater than 8 (*i.e.* the value obtained for plain Cl$^-$ anions), as shown in Fig. 3c.

The remaining two compounds, $Imma$-Na_2Cl and $R\bar{3}$-Na_4Cl_3, are characterized by the absence of polysynaptic ELF basins. The valence ELF distribution is concentrated around Cl atoms (Fig. S8b, ESI†). Yet the DOS plots (Fig. 5a and Fig. S10, ESI†) indicate that these compounds are metallic. The question is therefore raised as to what is the chemical origin of their metallic character. The broad band which confers to these compounds their metallic character is formed by d-orbitals of chlorine. Moreover, the plot of charge density relative to such band shows the formation of a network of Cl–Cl bonds (Fig. 5b and c and Fig. S10, ESI†).

All these results delineate, for very high-pressure alkali subhalides, a chemical bonding picture in which all the valence electrons of sodium are transferred to chlorine. The extra electrons, with respect to the one required for the completion of Cl octet configuration, give rise to Cl–Cl bonds formed by d-orbitals. This, however, would imply that the Cl atoms in $Imma$-Na_2Cl are in the previously unobserved −2 oxidation state. To understand whether this is the case, we analyze the Cl charge in both ELF and QTAIM frameworks. Within the latter approach, which usually gives charges lower than the formal oxidation state, we observe an increase of +76% with

respect to the value obtained for NaCl at the same pressure (Table 1). The integration of charge density within Cl monosynaptic basins puts the final word on the issue: the total electron population sums up to 9.0 (Fig. S8b, ESI†), leading to a −2.0 charge. Equivalent results were obtained by using hybrid and meta-GGA DFT Hamiltonians (Table S10, Fig. S29 and S30, ESI†). The numerous Na$^+$ atoms (Fig. 1d) surrounding each Cl^{2-} certainly play an important role in stabilizing such an unusually high charge. It is worth noticing that $Imma$-Na_2Cl adopts the CaCu$_2$ structure, which is common to numerous alloys.[31] The chemical bonding picture described so far is found in Na_4Cl_3 (Fig. S10, ESI†) and $Cmmm$-Na_3Cl_2 (Fig. S11, ESI†) as well, although the Cl-d valence band is clearly less populated due to the different stoichiometry. However, the very high-pressure phase of Na_3Cl_2, *hitherto* believed to be thermodynamically stable above 260 GPa, decomposes exothermically into Na_4Cl_3 + Na_2Cl (36 meV per atom at 300 GPa). Na_3Cl, instead, does not form similar structures within the investigated pressure range, because it would require Cl to be in the unfavorable −3 oxidation state. This is clearly highly energetically unfavorable and an extremely high pressure is allegedly required for its formation.

3.2. Sodium subchlorides: high-pressure stability

In this section, we discuss the stability of sodium subchlorides in the context of the chemical bonding patterns presented above. Normally, for pressure-driven reactions and phase transitions, it is the volume reduction that is responsible for the product stability (by lowering the pV term), whereas the

2844 | *Phys. Chem. Chem. Phys.*, 2016, **18**, 2840–2849

This journal is © the Owner Societies 2016

internal energy change is unfavorable.¶ Sodium subchlorides are no exception, as shown in Table S3 (ESI†). Fig. 2 schematically shows that, as pressure rises, Na_xCl ($1 < x \leq 3$) compounds generally evolve through the following sequence of structures: NaCl + $(x - 1)$Na (separate phases, no reaction) → Na_xCl phases containing 2D-Na layers → phases with 1D-Na strands → phases without Na–Na bonds (only for $x \leq 2$). Note that this sequence corresponds to the progressive breaking of metallic bonds, namely in one, two and three dimensions, and to the formation of Na/NaCl interfaces. For a given stoichiometry, such phase transitions are invariably accompanied by an increase in the anion–cation coordination∥ (*i.e.* the number of sodium atoms in the coordination sphere of chlorine) as reported in Fig. 2 and shown in Fig. S5 and S14 (ESI†). Below, we show that a direct correlation exists between the formation of additional Na⋯Cl contacts and the volume reduction.

Let us start by considering the reaction 2Na + NaCl → $P4/mmm$-Na_3Cl. The structure of the product can be divided into Na-bcc and NaCl blocks (Fig. 6a). The crystal volume may be partitioned accordingly and the resulting block volumes can be compared to those in pure Na and pure NaCl. Atomic volume of Na is similar in pure Na and in Na-bcc blocks of Na_3Cl. The slight expansion in passing from the former to the latter is likely due to the electron depletion within the 2D-Na layers (see previous section), which weakens the Na–Na metallic bonds. The volume reduction associated to the Na_3Cl formation takes place mainly within the NaCl units. The origin of this shrinking can be understood by comparing the coordination sphere of Cl anions in pure NaCl to that of NaCl units in the $P4/mmm$ structure. In the latter, the environment of Cl atoms can be viewed as a CsCl structure (*i.e.* the one adopted by NaCl at this pressure) where two neighboring anions have been substituted by cations. Clearly, the replacement of an anion⋯anion contact by a cation⋯anion interaction is expected to induce a distance shortening. This is indeed the case: both NaCl and Na-bcc blocks are flattened along the direction perpendicular to Na/NaCl interface, *i.e.* the direction of the additional Na⋯Cl interactions (see Fig. 6a). Moreover, this flattening increases with pressure (Table S4, ESI†). Therefore, one can conclude that the volume reduction associated to Na_3Cl formation is induced by the anion–cation coordination increase. The same is expected to hold true for the transition from 2D-Na to 1D-Na sublattices. To demonstrate this, we consider the $Cmmm$ and $P4/mmm$ structures of Na_2Cl (Fig. 6b and c). $P4/mmm$, although not thermodynamically stable, is the lowest-enthalpy phase of Na_2Cl below 125 GPa and features a 2D-Na sublattice. Above such pressure, the $Cmmm$ structure (1D-Na sublattice) becomes more enthalpically favorable and Na_2Cl becomes thermodynamically stable. Since both phases can be partitioned into Na and NaCl
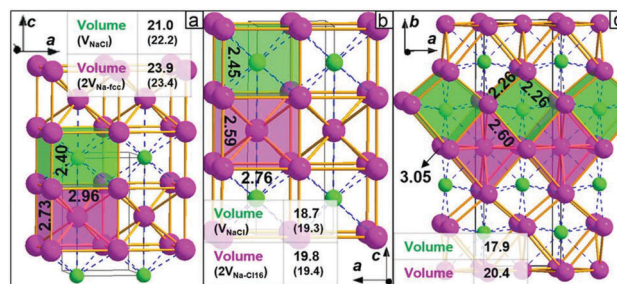

Fig. 6 Crystal structures and block partitioning for Na_xCl compounds. Bond lengths (Å) and subdivision into Na-bcc (violet) and NaCl (green) blocks are reported for $P4/mmm$-Na_3Cl at 80 GPa (a), $P4/mmm$-Na_2Cl at 135 GPa (b) and $Cmmm$-Na_2Cl at 135 GPa (c). In all pictures, the blocks are prisms whose height is parallel to the c crystallographic axis. In (a) and (b) the bases are squares for both blocks, whereas in (c) the bases are rhombi (Na-bcc) and kites (NaCl). The tables reports the volume (Å³) of the blocks of the corresponding color. In (a) and (b), the numbers in brackets indicate the volume of an equivalent number of atoms of pure NaCl and of pure Na (in their most stable phase) at the same pressure.

blocks, they represent an ideal case to test the abovementioned hypothesis. The $P4/mmm$ → $Cmmm$ transition, associated to an anion–cation coordination increase (Fig. 6b and c), is expected to induce a further shrinking of the NaCl blocks. This is exactly what happens, as it can be seen from Fig. 6b and c. Moreover, both Na-bcc and NaCl blocks are shorter in the two directions perpendicular to the Na/NaCl interface, thereby further corroborating the role played by Na⋯Cl interactions in leading to the volume reduction (see also Fig. S12 and S14, ESI†). For Na_3Cl, the 2D-Na → 1D-Na sublattice transformation takes place along the $P2_1/c$ → $R\bar{3}m$ transition. In Fig. S14 (ESI†) we show how, also for this transition, the associated volume reduction takes place within the NaCl blocks. All these results establish that in the formation of Na_xCl compounds with 2D-Na layers and in their phase transition to phases with 1D-Na strands, the volume reduction is achieved through the anion–cation coordination increase. Such increase takes place also in passing from structures with 1D-Na sublattices to those containing no Na–Na bonds, namely $Imma$-Na_2Cl and $R\bar{3}$-Na_4Cl_3 (the metastable, lowest-enthalpy phase of Na_4Cl_3 below 170 GPa is reported in Fig. S13 (ESI†), where its 1D-Na sublattice is shown). We conclude that also for these phase transitions the volume reduction is achieved through the formation of additional Na⋯Cl interactions.

Finally, we note that Na_3Cl displays a transition ($P4/mmm$ → $P2_1/c$) where the dimensionality of the sublattice does not charge (2D-Na). In agreement with the discussion above, the anion–cation coordination number remains constant as well, and the volume reduction takes place within the 2D-Na layers (Fig. S14, ESI†). The latter rearrange so as to produce a more compact geometry. This observation complies with the more localized character of Na metallic bonds in $P2_1/c$-Na_3Cl (see previous section). This phase transition is a peculiarity of the Na/Cl system, it will be discussed in the next section in comparison with other alkali subhalides.

In summary, pressure-induced phase transitions of sodium subchlorides are generally accompanied by metallic bonds

¶ The enthalpy variation associated to a given reaction at constant pressure is given by $\Delta H = \Delta U + p\Delta V$, where H is the enthalpy, U is the internal energy, V is the volume, and p the external pressure.

∥ Note that, on the contrary, the total coordination number of chlorine atoms remains constant along two phase transitions (namely Na_4Cl_3-$P2/m$ → Na_4Cl_3-$R\bar{3}$ and $P4/mmm$-Na_2Cl → $Cmmm$-Na_2Cl) and along the reaction NaCl + 2Na → $P4/mmm$-Na_3Cl.

breaking and consequent Na/NaCl interface formation, by internal energy rise, by volume reduction and by anion–cation coordination increase. The latter two features were shown to be entangled. Overall, we can highlight two main factors determining the stability of sodium subchlorides at high pressure:

• *The increase of the anion–cation coordination number.* The formation of additional Na···Cl interactions induces a volume reduction, thereby favoring the pV term in the enthalpy expression.

• *The making/breaking of metallic bonds between alkali atoms.* The breaking of metallic bonds or, equivalently, the formation of a Na/NaCl interface, rises the internal energy. This bond cleavage, on the other hand, is to take place in order to allow the increase in the anion–cation coordination number.

The applied external pressure has the effect of changing the balance between the above two factors, by making the pV term progressively more important and leading to the observed sequence of phases. Below we test this model on other chemical systems.

3.3. Newly predicted structures of alkali subhalides

In this section we exploit the results of our crystal structure predictions to investigate the energetics of the following reaction:

$$2A + AY \rightarrow A_3Y \quad (A = Li, Na, K; Y = F, Cl, Br) \quad (2)$$
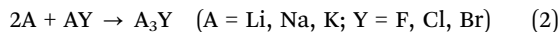
in the pressure range 0–350 GPa. We label as 'stable' the lowest-enthalpy structures for which reaction (2) is exothermic. Note that, for a given A_3Y compound, the exothermicity of this reaction is a necessary, but not sufficient condition for its thermodynamical stability. However, it does predict the formation of at least one alkali subhalide A_xY ($x > 1$). Reaction (2) turns out to be exothermic for all the investigated alkali subchlorides and subbromides (Table 2), whereas no alkali subfluorides are predicted to form below 350 GPa. As shown below, this is because fluorine is, compared to other halogens, exceptionally small[32] (and scarcely compressible[33]). A more important goal of this analysis is to test whether the compounds resulting from reaction (2) follow the model derived in the previous section. According to the latter, we anticipate A_3Y compounds to form phases with 2D metallic bonding between alkali atoms. As pressure increases, we expect a transition towards 1D metallic bonds, accompanied by an increase in the anion–cation coordination. For Li_3Cl, Li_3Br and Na_3Br we observe all these features, as explained in the following. At low pressure, these subhalides are isostructural to Na_3Cl ($P4/mmm$ space group), and according to ELF, valence and deformation density distributions, the chemical bonding patterns of these 4 compounds are identical (Fig. S17 and S18, ESI†). Upon pressure increase, Li_3Cl, Li_3Br and Na_3Br all undergo a phase transition to form a 'Cu3Au' structure ($Pm\bar{3}m$ space group, Fig. 7a). Note that for Li_3Br, reaction (2) occurs at higher pressure than the $P4/mmm \rightarrow Pm\bar{3}m$ transition, hence $P4/mmm$-Li_3Br is metastable. The Cu3Au structure can be viewed as composed of 1D-Na (1D-Li) sublattices crossing each other in a 3-dimensional network (Fig. 7b and c). Accordingly, their ELF and charge density distributions manifest all the typical features observed for Na_xCl compounds with 1D-Na sublattices (Fig. S18b and Table S9, ESI†). Both quantities

Table 2 Formation and phase transition pressures of investigated compounds in the range 0–350 GPa

Compound	Stability[a]	Phase transitions[b]
Li_3Cl	52 GPa	$P4/mmm\|Pm\bar{3}m$: 57 GPa
Li_3Br	34 GPa	$P4/mmm\|Pm\bar{3}m$: 19 GPa
Na_3Br	36 GPa	$P4/mmm\|Pm\bar{3}m$: 83 GPa
		$Pm\bar{3}m\|R\bar{3}m$: 250 GPa
K_3Cl	77 GPa	$Pm\bar{3}m\|I4/mmm$: 95 GPa
K_3Br	48 GPa	$Pm\bar{3}m\|R\bar{3}m$: 70 GPa
		$R\bar{3}m\|C2/m$: 193 GPa

[a] Pressure at which the reaction $AY + 2A \rightarrow A_3Y$ (A = Li, Na, K; Y = Cl, Br) becomes exothermic. [b] Pressure required for each phase transition.

exhibit maxima at the center of octahedral cavities within the 1D-Na (1D-Li) sublattice, *i.e.* at the 1b Wyckoff position (0.5, 0.5, 0.5). On top of that, the valence DOS displays a rather sharp peak, whose density is localized around the ELF/charge density maxima just mentioned (Fig. 8a and Fig. S19, ESI†). Note that, above 250 GPa, the Cu3Au structure of Na_3Br undergoes a slight distortion (Fig. S16, ESI†), which lowers its symmetry to $R\bar{3}m$.

As expected, the formation of $P4/mmm$ structures and their transition to $Pm\bar{3}m$ phases are associated to an increase in the anion–cation coordination number (from 8 to 10, and from 10 to 12), which leads to stabilization due to volume reduction (Tables S5 and S7, ESI†). Clearly, for this coordination increase to take place, the cations are to densely pack around the anion. Consequently, they will experience some degree of repulsion. The smaller (bigger) is the anion (cation), the higher such repulsion is expected to be. Therefore, we anticipate the differences in the behavior of the various lithium and sodium subhalides to be explicable on the basis of simple steric arguments. To that purpose, we show the anion/cation radius ratios in Table 3.**[34] Alkali subfluorides display a very small ratio. This explains why they are not stable within the investigated pressure range. For the remaining four alkali subhalides, a rough inverse proportionality is observed between the radius ratios and the pressure required for the formation of phases with 1D-Na (1D-Li) sublattice.

These facts corroborate the relationship between ions dimension, anion–cation coordination increase and high-pressure
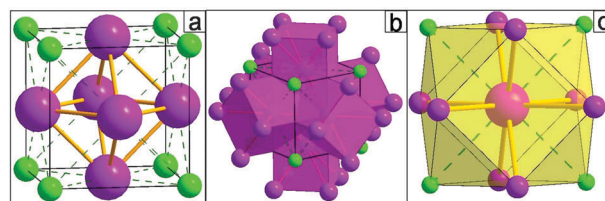

Fig. 7 $Pm\bar{3}m$ structure formed by alkali subhalides. In (a), the cubic unit cell is displayed. In (b), we show how this structures can be seen as a 3-dimensional net of 1D-Na (or 1D-Li) strands formed by elongated bcc blocks (colored in violet). This concept can be understood more clearly from (c), where the coordination sphere of an alkali atom, forming a cuboctahedron, is displayed. The six square faces are perpendicular to the three crystallographic axes. In two directions, the corresponding four faces are formed by both alkali and halogen atoms. In the third direction, the two faces are formed by alkali atoms only. This very direction is the one along which the elongated bcc blocks extend throughout the crystal.
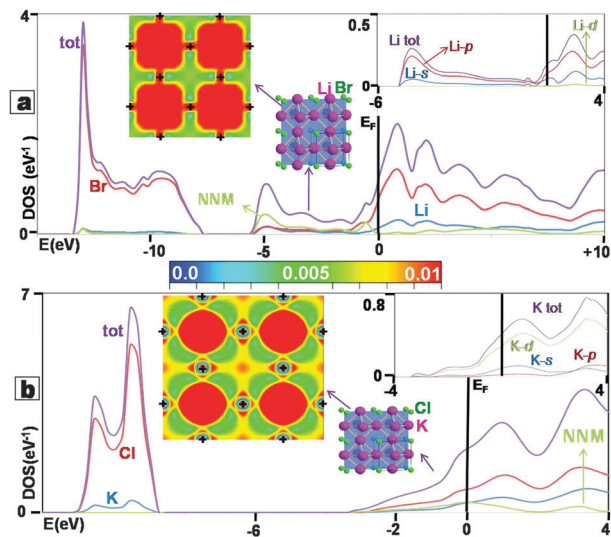
Paper

Fig. 8 p-DOS plots and valence density distribution for $Pm\bar{3}m$ structures of Li$_3$Br (a) and K$_3$Cl (b) at 100 GPa. NNM indicates the contribution from the basis centered on non-nuclear maxima. The insets at the center of each picture shows the valence density (e Bohr^{-3}) plotted onto the (100) plane (2 × 2 supercell). The positions of halogen atoms are indicated as black crosses, whereas the color scale is reported in the center of the picture. The upper right insets show the orbital decomposition of alkali contributions as obtained from the calculation where no basis were included on the NNM.

stability. Na–Cl ratio lies in between the one of alkali subfluorides and that of the remaining subhalides. Accordingly, the phase diagram of Na$_3$Cl presents two main differences with respect to that of Li$_3$Cl, Li$_3$Br and Na$_3$Br. First, its structure with 1D-Na sublattice is substantially more distorted (Fig. 1e *vs.* Fig. 7). Second, only for Na$_3$Cl is the $P2_1/c$ structure stable. For other alkali subhalides, such structure does become more stable than the $P4/mmm$ at a certain pressure†† (because of the volume reduction within 2D-Na/2D-Li layers discussed in the previous section). However, at a lower pressure, Li$_3$Cl, Li$_3$Br and Na$_3$Br achieve a more efficient overall volume reduction by increasing their anion–cation coordination, *i.e.* by forming 1D-Li/1D-Na sublattices ($Pm\bar{3}m$ phase). For Na$_3$Cl, due to the unfavorable ions size, such process requires a considerably greater pressure, below which the $P4/mmm \rightarrow P2_1/c$ transition takes place.

Potassium subhalides display a sequence of high-pressure phases which cannot be rationalized on the basis of the model proposed above. At low pressure, K$_3$Cl and K$_3$Br form the Cu$_3$Au structure already observed for other subhalides (Table 2). Above 100 GPa, both K$_3$Cl and K$_3$Br undergo transitions to phases different from the ones discussed so far (*vide infra*).

** We adopted the ionic radii (the largest among the ones reported for each atom type) obtained by Waber and Cromer (ref. 34). Qualitatively equivalent results were obtained by using the pseudopotential radii calculated by Zunger (ref. 32), whose model was in turn based on the popular approach put forward by Simons and Bloch, see Table S8 (ESI†).

†† The pressures required for this phase transition are 150 and 240 GPa for Na$_3$Br and Li$_3$Br, respectively. For Li$_3$Cl, a similar transition occurs at 405 GPa, although at such pressure the $P2_1/c$ structure has already undergone a second-order phase transition to a $I4/mmm$ structure (isostructural to the one of K$_3$Cl).

Table 3 Anion/cation radius ratios for lithium and sodium halides

	F	Cl	Br
Li	2.12	3.93	4.60
Na	1.44	2.67	3.13

The $P4/mmm$ structure, instead, is not energetically competitive at any pressure. In the following, we uncover the reasons behind the peculiar behavior of potassium subhalides by analyzing their crystal and electronic structures. In Fig. 8, we contrast the DOS and valence density distribution of Li$_3$Br with those of K$_3$Cl, both compounds in their Cu$_3$Au ($Pm\bar{3}m$) phase. Important differences emerge. Whereas for Li$_3$Br the valence and conduction bands are well distinguishable in the DOS plots, K$_3$Cl exhibits a more metal-like DOS containing sizeable contributions from both potassium and chlorine atoms (K$_3$Br gives similar results, Fig. S20, ESI†). Correspondingly, the accumulation of valence density around the 1b Wyckoff position of K$_3$Cl is not as marked as in lithium and sodium subhalides. In particular, a significant portion of the valence density of K$_3$Cl lies in the octahedral cavities formed by 4 K and 2 Cl atoms (Fig. 8b, inset). The QTAIM analysis reflects these differences: the charges relative to the non-nuclear maxima in K$_3$Cl and K$_3$Br are about one order of magnitude lower than in the Cu$_3$Au structure of the remaining alkali subhalides (Table S9, ESI†). Another important difference is that d-orbitals, negligibly populated for lithium and sodium, constitute the major part of the potassium contribution to the valence band (Fig. 8a and b, insets). Overall, these results indicate a significant, pressure-induced, potassium–halogen hybridization. As pressure rises, the Cu$_3$Au structures of potassium subhalides transform into the phases represented in Fig. 9. Their potassium sublattices cannot be classified as 2D or 1D, as their chemical bonding pattern is somewhat more complex.

For K$_3$Cl, we recovered the $I4/mmm$ phase reported in ref. 24 (Fig. 9a). We note that this structure can be obtained from $Pm\bar{3}m$ by sliding the Cl-containing (100) plane along the bc diagonal, which leads to the disruption of each K$_6$ octahedron (which composes the 1D-K sublattice in $Pm\bar{3}m$) to form two K$_5$Cl octahedra. These structural changes suggest that K$_3$Cl attains its high-pressure stability by favoring the K–Cl hybridization. The DOS analysis supports this hypothesis. Along the phase $Pm\bar{3}m \rightarrow I4/mmm$ phase transition, the relative potassium contribution to the valence band increases (Fig. S21, ESI†). More importantly, we observe that its valence density is mostly accumulated inside K$_5$Cl octahedral cavities (Fig. 10), *i.e.* K–Cl multicenter bonds are formed.

$R\bar{3}m$ and $C2/m$ phases of K$_3$Br are structurally and energetically similar (the enthalpy difference is 18 meV per atom at 250 GPa). In particular, they are both formed by quite flat layers of potassium intersecting each other and enclosing Br anions. In passing from Cu$_3$Au to high-pressure structures, the relative contribution of potassium to the valence band increases, and so do its s- and p-orbitals components (Fig. S21, ESI†). In both $R\bar{3}m$ and $C2/m$ phases the valence density is mostly accumulated along the K–K internuclear axis (Fig. S22, ESI†) and K–K bonds shorter than in the Cu$_3$Au structure are formed (Fig. S23, ESI†).

This journal is © the Owner Societies 2016

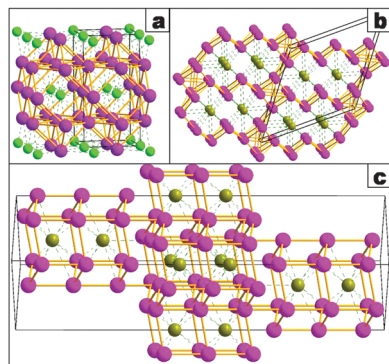*Phys. Chem. Chem. Phys.*, 2016, **18**, 2840–2849 | **2847**

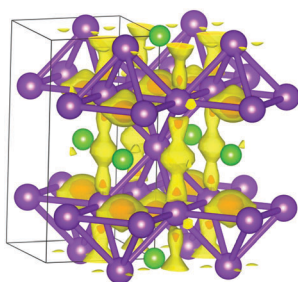Fig. 9   Structures of $I4/mmm$-K_3Cl (a), $C2/m$-K_3Br (b) and $R\bar{3}m$-K_3Br (c).

Fig. 10   Valence density distribution of $I4/mmm$-K_3Cl. Isovalues: 0.011 a.u. (yellow) and 0.013 a.u. (red). The orientation is similar to that of Fig. 9a.

This indicates the formation of stronger K–K bonds taking place through spd hybridization.

Finally, we note that polysynaptic ELF basins could not be detected in K_3Cl, K_3Br and high-pressure (>100 GPa) allotropes of pure K,‡‡ even though these compounds are clearly metallic. We conclude that the presence of polysynaptic ELF basins is not required for metallic bonds in high-pressure potassium.

In summary, the model we put forward in the previous section correctly predicts the structural evolution and the chemical bonding pattern of lithium and sodium subhalides at high pressure. Conversely, potassium subhalides deviates from the expected high-pressure behavior, due to the participation of d-orbitals in the chemical bonding and to the K–halogen hybridization. The involvement of d-orbitals is not completely unexpected, as it was already observed in previous DFT studies on the high-pressure allotropes of pure K, Rb and Cs.[35] More generally, pressure-induced stabilization of d-orbitals compared to s- and p-orbitals has been demonstrated by different *ab initio* approaches.[36,37]

3.4.   General implications for high-pressure chemistry

The stability factors outlined for alkali subhalides are expected to hold true for a broad range of compounds. In fact, for ionic systems under high pressure, we foresee the formation of

compounds with a stoichiometric excess of cations to be more a rule rather than an exception. However, for certain compounds, factors other than the ones discussed above might play an important role, too (as it happens, for example, for potassium subhalides). Conversely, binary compounds formed by Li, Be, Na and Mg with elements of the groups 15, 16, 17 and possibly also 13 and 14, will closely mimic the high-pressure behavior observed for lithium and sodium subhalides. In order to test this hypothesis, we scrutinized the literature and sought studies on the high-pressure behavior of ionic systems. We selected three systems: Na/Bi,[38] Li/B,[39,40] and Mg/O.[41] Within Mg_3O_2, stable above 400 GPa, Mg atoms form a 1D-Mg sublattice composed of Mg-bcc blocks and enclosing non-nuclear maxima within distorted octahedral cavities. Accordingly, a sharp peak is found in the valence DOS. These features closely resemble those of alkali subhalides with 1D sublattices. Concerning Na/Bi and Li/B systems, we performed DFT calculations in order to analyze their DOS and valence density distribution. Two Na_xBi ($x > 3$) compounds are stable at high pressure: Na_4Bi and Na_6Bi. Above 140 GPa, Na_6Bi forms an oP14 phase, which transforms to hR21 as pressure rises. In the former structure, sodium forms a 2D pattern of metallic bonds, whereas in the latter the valence band is more peak shaped and the corresponding density more localized (Fig. S24, ESI†), as it happens in subhalides composed of 1D-Na sublattices. The transition is accompanied by an increase in the anion–cation coordination (16 to 18). Thus, Na_6Bi behaves exactly as predicted by our model. Na_4Bi, instead, forms only one phase, containing a 1D-Na sublattice, consistent with its rather flat valence bands (Fig. 9c of ref. 38). Within the rich Li/B phase diagram, we analyze the Li-richest compound displaying a phase transition: Li_5B. Between 20 and 90 GPa, two lowest-enthalpy structures ($P2_1/m$ and $P\bar{1}$), differing by a few meV per atom, were predicted. They contain both B–B and Li–Li bonds, and their anion–cation coordination number is the same (12), as shown in Fig. S25 and S26 (ESI†). Above 90 GPa, a phase transition occurs (to $Cmma$ structure§§), which leads to an anion–cation coordination increase and to the disruption of Li–Li and B–B bonds (Fig. S27, ESI†). All the valence electrons are then employed for forming unusual B^{5-} anions. This process is reminiscent of what happens for the very high-pressure phases of Na_xCl ($x = 1.33, 1.5, 2$), the difference lying in the anions orbitals which are filled: Cl–Cl bonding for Na_xCl, B–B antibonding for Li_5B. Overall, we have demonstrated how the model we derived for explaining the high-pressure behavior of alkali subhalides can be exploited to rationalize the cation-rich part of the Mg/O, Na/Bi and Li/B phase diagrams. As a final note, it should be mentioned that for heavy atoms, a more complex chemical behavior is to be expected, which might lead to the formation of metal-rich compounds even at ambient pressure (for example, cesium and rubidium suboxides Rb_xO and Cs_xO, $x = 4$–7[42]).

---

‡‡ For the two highest-pressure allotropes of potassium reported in ref. 24, oc16 and dhcp (space group $Cmcm$ and $P6_3/mmc$, respectively), we detected tiny interstitial basins whose maximum ELF values are 0.24 and 0.19, respectively. Clearly, such a picture cannot be considered as an indication of metallic bond. Yet their DOS indicate that these phases are metallic.

§§ Actually, another phase ($Cmcm$ space group) was reported to be slightly more stable (ref. 40) in the pressure range 90–110 GPa. However, $Cmcm$ and $Cmma$ display similar DOS, valence density distribution, and anion–cation coordination (Fig. S27 and S28, ESI†).

4. Conclusions

We have presented an in-depth investigation on the high-pressure stability of alkali subhalides, carried out by means of an evolutionary crystal structure prediction technique (USPEX code[7]) combined with quantum-mechanical calculations. For previously reported[2] sodium subchlorides Na_xCl ($x > 1$), we have discovered their phase diagram to be richer than previously thought. Their chemical bonding was thoroughly investigated, and it was shown to exhibit features not observed in any ambient-pressure compound. More importantly, we derived a predictive model by singling out those factors which determine the stability of Na_xCl under pressure. We performed crystal structure prediction calculations on alkali subhalides A_3Y (A = Li, Na, K; Y = F, Cl, Br) in order to test this model. The latter correctly anticipates the main structural and electronic features of lithium and sodium subhalides, but for potassium compounds we find a more complex picture due to involvement of d-orbitals. Finally, we showed how the insights gained in the present study can be used to rationalize the stability of recently discovered high-pressure compounds. Overall, this work represents one of the first steps in the construction of predictive models for high-pressure chemistry, up to now scarcely existing.

Acknowledgements

References

1 W. Grochala, R. Hoffmann, J. Feng and N. W. Ashcroft, *Angew. Chem., Int. Ed.*, 2007, **46**, 3620–3642.
2 W. Zhang, A. R. Oganov, A. F. Goncharov, Q. Zhu, S. E. Boulfelfel, A. O. Lyakhov, E. Stavrou, M. Somayazulu, V. B. Prakapenka and Z. Konopkova, *Science*, 2013, **342**, 1502–1505.
3 Q. Zhu, D. Y. Jung, A. R. Oganov, C. W. Glass, C. Gatti and A. O. Lyakhov, *Nat. Chem.*, 2013, **5**, 61–65.
4 Y. Ma, M. Eremets, A. R. Oganov, Y. Xie, I. Trojan, S. Medvedev, A. O. Lyakhov, M. Valle and V. Prakapenka, *Nature*, 2009, **458**, 182–185.
5 M.-S. Miao, *Nat. Chem.*, 2013, **5**, 846–852.
6 C. T. Prewitt and R. T. Downs, *Rev. Mineral.*, 1998, **37**, 283–317.
7 A. R. Oganov and C. W. Glass, *J. Chem. Phys.*, 2006, **124**, 244704.
8 R. F. W. Bader, *Atoms In Molecules: A Quantum Theory*, Clarendon press, Oxford, 1990.
9 A. D. Becke and K. E. Edgecombe, *J. Chem. Phys.*, 1990, **92**, 5397–5403.
10 C. Gatti, *Z. Kristallogr.*, 2005, **220**, 399–457.
11 A. Savin, B. Silvi and F. Colonna, *Can. J. Chem.*, 1996, **74**, 1088–1096.
12 J. P. Perdew, K. Burke and M. Ernzerhof, *Phys. Rev. Lett.*, 1996, **77**, 3865–3868.
13 P. E. Blöchl, *Phys. Rev. B: Condens. Matter Mater. Phys.*, 1994, **50**, 17953–17979.

14 G. Kresse and J. Furthmuller, *Comput. Mater. Sci.*, 1996, **6**, 15–50.
15 R. Dovesi, R. Orlando, A. Erba, C. M. Zicovich-Wilson, B. Civalleri, S. Casassa, L. Maschio, M. Ferrabone, M. De La Pierre, P. D'Arco, Y. Noel, M. Causa, M. Rerat and B. Kirtman, *Int. J. Quantum Chem.*, 2014, **114**, 1287–1317.
16 M. F. Peintinger, D. V. Oliveira and T. Bredow, *J. Comput. Chem.*, 2013, **34**, 451–459.
17 O. Otero-de-la-Roza, E. R. Johnson and V. Luaňa, *Comput. Phys. Commun.*, 2014, **185**(3), 1007–1018.
18 M. Yu and D. R. Trinkle, *J. Chem. Phys.*, 2011, **134**, 064111.
19 A. O. Lyakhov, A. R. Oganov, H. T. Stokes and Q. Zhu, *Comput. Phys. Commun.*, 2013, **184**, 1172–1182.
20 A. R. Oganov, A. O. Lyakhov and M. Valle, *Acc. Chem. Res.*, 2011, **44**(3), 227–237.
21 J. Lv, Y. Wang, L. Zhu and Y. Ma, *Phys. Rev. Lett.*, 2011, **106**, 015503.
22 V. F. Degtyareva and O. Degtyareva, *New J. Phys.*, 2009, **11**, 063037.
23 Y. Ma, A. R. Oganov and Y. Xie, *Phys. Rev. B: Condens. Matter Mater. Phys.*, 2008, **78**, 014102.
24 W. Zhang and A. R. Oganov, Stability of numerous novel potassium chlorides at high pressure, unpublished work.
25 X. Chen and Y. Ma, *EPL*, 2012, **100**, 26005.
26 A. Shamp, P. Saitta and E. Zurek, *Phys. Chem. Chem. Phys.*, 2015, **17**, 12265.
27 A. Togo, F. Oba and I. Tanaka, *Phys. Rev. B: Condens. Matter Mater. Phys.*, 2008, **78**, 134106.
28 Diamond 3.2h, Copyright (c) 1997–2012 Crystal Impact GbR, Bonn Germany, by Klaus Brandenburg.
29 K. Momma and F. Izumi, *J. Appl. Crystallogr.*, 2011, **44**, 1272–1276.
30 B. Silvi and C. Gatti, *J. Phys. Chem. A*, 2000, **104**, 947–953.
31 G. Nuspl, K. Polborn, J. Evers, A. G. Landrum and R. Hoffmann, *Inorg. Chem.*, 1996, **35**, 6922–6932.
32 A. Zunger, *Phys. Rev. B: Condens. Matter Mater. Phys.*, 1980, **22**, 5839–5872.
33 A. Martin-Pendas, A. Costales, M. A. Blanco, J. Recio and V. Luana, *Phys. Rev. B: Condens. Matter Mater. Phys.*, 2000, **62**(21), 13970–13978.
34 J. T. Waber and D. T. Cromer, *J. Chem. Phys.*, 1965, **42**, 4116.
35 Y. Ma, A. R. Oganov and Y. Xie, *Phys. Rev. B: Condens. Matter Mater. Phys.*, 2008, **78**(1), 014102.
36 M.-S. Miao and R. Hoffmann, *Acc. Chem. Res.*, 2014, **47**, 1311–1317.
37 H. E. Montgomery Jr. and V. I. Pupyshev, *Phys. Lett. A*, 2013, **377**, 2880–2883.
38 X. Cheng, R. Li, D. Li, Y. Li and X.-Q. Chen, *Phys. Chem. Chem. Phys.*, 2015, **17**, 6933–6947.
39 A. Hermann, A. McSorley, N. W. Ashcroft and R. Hoffmann, *J. Am. Chem. Soc.*, 2012, **134**, 18606–18618.
40 F. Peng, M.-S. Miao, H. Wang, Q. Li and Y. Ma, *J. Am. Chem. Soc.*, 2012, **134**, 18599–18605.
41 Q. Zhu, A. R. Oganov and A. O. Lyakov, *Phys. Chem. Chem. Phys.*, 2013, **15**, 7696–7700.
42 A. Simons, *Struct. Bonding*, 1979, **36**, 81–127.

This journal is © the Owner Societies 2016

Phys. Chem. Chem. Phys., 2016, **18**, 2840–2849 | **2849**